

Optical transport of cold atoms to quantum degeneracy

Yanqing Tao, Yufei Wang, Ligeng Yu, and Bo Song*

*State Key Laboratory for Mesoscopic Physics and Frontiers Science Center for Nano-optoelectronics,
School of Physics, Peking University, Beijing 100871, China*

Efficient transport of cold atoms is essential for continuous operation, enabling applications ranging from atomic lasers to continuously operated qubits. However, deep potentials required to overcome vibrations, axial trap nonuniformity and insufficient cooling have limited transport of cold atoms near quantum degeneracy. Here we demonstrate rapid optical transport of cold atoms to Bose-Einstein condensation using a moving optical lattice formed by two Bessel beams. A gas of 3×10^5 ytterbium atoms at a temperature of 340 nK is transported over 34 cm in 350 ms with efficiency over 60%. Furthermore, a degenerate gas of 1×10^5 atoms with a 40% condensate fraction emerges from the phase synchronization process driven by atomic interactions. This demonstration enables the fast preparation of ultracold atomic beams and large-scale atom arrays for quantum sensing, simulation and computing.

I. INTRODUCTION

Atom transport has been widely employed to deliver atoms into better vacuum conditions for longer lifetimes. It also plays a crucial role in the preparation and continuous loading of cold atoms for applications ranging from atom lasers in quantum sensing to atomic qubits in quantum simulation and computing [1–5]. Although transport has been experimentally demonstrated using different methods including magnetic [6–12], optical [13–22], and hybrid schemes [23, 24], fast transport of cold atoms near degeneracy over long distances remains challenging, due to vibrations, nonuniform potentials along the transport and insufficient cooling.

In this letter, we demonstrate the transport of cold atoms using a moving optical lattice formed by two Bessel beams with precise control. Owing to the properties of Bessel beams, their extended nondiffracting range along the transport direction exceeds that of Gaussian beams of the same beam size, allowing for more uniform and shallower potentials for transporting colder atoms. We manage to transport a gas of 3×10^5 ytterbium (Yb) atoms at 340 nK over 34 cm in 350 ms, with position control accuracy of 2 μm over the whole transport.

Eventually a degenerate gas of 1×10^5 atoms with a 40% condensate fraction is produced through collision thermalization followed by a phase synchronization process. By both decelerating the moving lattice and lowering the trap potential in the final stage, the hotter atoms are spilled out from each pancake trap in the moving lattice. Notably, the deceleration effectively lowers the trap depth, but the trap frequencies remain high, maintaining a high atomic density favorable for evaporative cooling. The moving lattice separates approximately 57 pancake-shaped clouds, each with a random phase resulting from independent collisional thermalization. After releasing the atoms into a shallow dipole trap, the phases of those pancakes are synchronized by atomic interactions within

a few hundred milliseconds, leading to Bose-Einstein condensation.

Our method not only enables rapid optical transport of cold atoms but also facilitates the fast realization of degenerate gases [25–27], and is broadly applicable to atom lasers and continuously operated large-scale atomic arrays [1–3].

II. EXPERIMENTAL SETUP

Fig. 1 shows the setup where cold atoms are transported over 34 cm between the magneto-optical trap (MOT) chamber and the science chamber which is a glass cell. Cold atoms are first prepared by a two-color MOT [28], followed by a compressed MOT to load atoms into a dipole trap, and short forced evaporative cooling to prepare different initial temperatures. Then, atoms are adiabatically loaded into the one-dimensional moving optical lattice by simultaneously ramping up the two counter-propagating Bessel beams to a lattice depth of $U/k_B \approx 15 \mu\text{K}$ with the Boltzmann constant k_B .

A key requirement for fast cold atom transport is that the moving optical lattice provides sufficient and uniform potential along the transport, in particular for cold atoms near quantum degeneracy which remains highly challenging due to sensitivity to vibrational noise and trap nonuniformity along the transport direction. For instance, magnetic transport relying on a series of coils typically restricts optical access, and technical noise and mechanical vibrations limit the achievable cold temperature [11]. On the other hand, transport based on tunable lenses typically has weak axial confinement and vibrational noise [16], while a moving optical lattice formed by Gaussian beams inevitably diverges over long transport distances and results in nonuniform trap potential along the transport [17–22].

To overcome the excessive diffraction of Gaussian beams over long distances, we employ Bessel beams which maintain a relatively uniform, diffraction-free trapping potential along the entire transport. The Bessel beam is generated by axicons [29] and the diffraction-

* bsong@pku.edu.cn

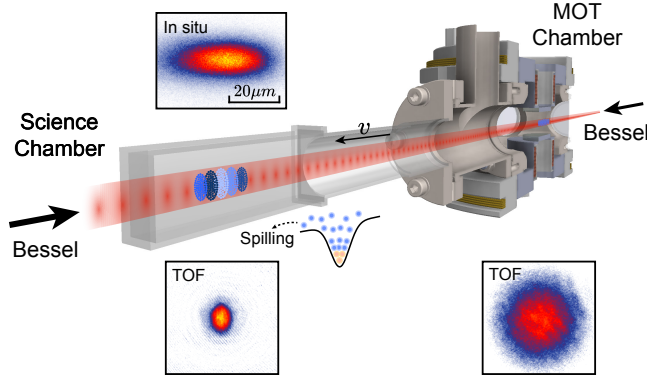


FIG. 1. Experimental setup. Cold ytterbium atoms are transported from a magneto-optical trap (MOT) chamber to a science chamber over a distance of 34 cm within 350 ms by a moving optical lattice formed by two counter-propagating Bessel beams. The lattice moves at a velocity of $v = \lambda\Delta f/2$ where λ is the lattice wavelength and Δf is the frequency difference between the two beams. The transport is precisely controlled by tuning the frequency difference. In the final stage of transport, the trap potential is tilted via deceleration and reduced by lowering the power, allowing hotter atoms to spill out and thereby evaporatively cooling the remaining atoms. Time-of-flight (TOF) images are taken after 15 ms and 20 ms of expansion in the MOT after loading and science chambers after phase synchronization, respectively.

free range is $z_{\max} = w_0 / \tan(\beta)$, where w_0 is the incident Gaussian waist and $\beta = (n - 1)\alpha$ with axicon apex angle α and refractive index n . The angle of axicon used in the experiment is 1° . The wavelength of the moving lattice is 1064 nm, far detuned from the $^1S_0 \rightarrow ^1P_1$ transition at 399 nm and the $^1S_0 \rightarrow ^3P_1$ transition at 556 nm of Yb atoms, thereby minimizing photon scattering and suppressing heating induced by the moving lattice. Two incident beams have powers of 14 W and 17 W, with beam waists of 2.5 mm and 3 mm, respectively. The resulting Bessel beams have central spot radii of $\sim 50 \mu\text{m}$, providing strong axial gradients against gravity. Fig. S4(a) in the Supplemental Material shows the details of the corresponding trap potential of the two individual beams, the total trap depth and lattice depth. In addition to its ability to handle higher optical power, this scheme is more power-efficient than Gaussian-beam transport. For the same transport distance of 34 cm, a Gaussian beam would require a beam waist of $240 \mu\text{m}$ to achieve a Rayleigh range of 17 cm, thereby significantly increasing the required optical power for trapping atoms.

The alignment of the moving lattice requires stringent procedures as the central waists of both Bessel beams are only $50 \mu\text{m}$. We developed a systematic procedure to align the moving lattice using multiple imaging techniques and lattice diffraction effect (see details in the Supplemental Material). Both the radial and lattice-induced axial confinement maintain the atomic cloud dense. The inset of Fig. 1 shows the atomic cloud size

at the end of transport detected by high-resolution insitu imaging.

The velocity of the moving lattice, $v = \lambda\Delta f/2$ is controlled by the frequency difference between two Bessel beams, where Δf is set by double-pass acousto-optic modulators (AOMs) and λ is the lattice wavelength. Transport of cold atoms begins with constant acceleration, followed by constant velocity transport and deceleration into the science chamber (see Supplemental Material for the detailed sequence). Since the axicons are purely static optical elements, our scheme has less vibration and technical noise than mechanical approaches using translation stages, rotating Moire lenses, or liquid tunable lenses. Our scheme provides precise positional control of the atoms. By comparing the designed motion curve with the measured center-of-mass of atoms, we achieved a correlation coefficient of $r^2 > 0.9999$ with corresponding maximum position residual less than half the camera pixel size. The actual transport motion precision is around $2 \mu\text{m}$ over long distance transport (see details in the Supplemental Material). After transport, atoms are loaded into a crossed dipole trap in the science chamber, where they are held for phase synchronization.

III. TRANSPORT AND EVAPORATION

Fig. 2 shows the calibration of the transport efficiency. Transport of cold atoms consists of three stages, initial loading, transport, and final unloading. Notably, when the lattice is accelerated or decelerated, the trapping potential of each pancake is tilted, effectively reducing the lattice depth while the trap frequencies remain high, a condition favorable for evaporative cooling. A similar method has been reported by evaporative cooling using magnetic gradient potential [30].

The initial loading temperature is controlled by varying the evaporation endpoint in the dipole trap. We characterize the temperature and efficiency of the transported atoms as functions of initial temperature in Fig. 2(a) and (b). The final temperature is less dependent on the initial temperature and approximately 340 nK. We further calibrate the overall transport efficiency at different positions by performing round-trip transport of the atoms, i.e. moving atoms back and forth over different distances in Fig. 2(c). Even after short round trips, atomic clouds with different initial conditions reach similar final temperatures, whereas hotter atoms are lost significantly, as reflected in the reduced transport efficiency. This initial atom loss originates from the population of higher lattice bands for hot temperatures. Subsequent acceleration effectively tilts the lattice potential, causing the hotter atoms to spill out. In the left panel of Fig. 2(d), we optimized the relative final atom number by varying the initial acceleration. For small accelerations, the atomic cloud suffers severe losses due to three-body interactions, while for larger accelerations, over-tilting of the lattice and heating also lead to decreased atom numbers.

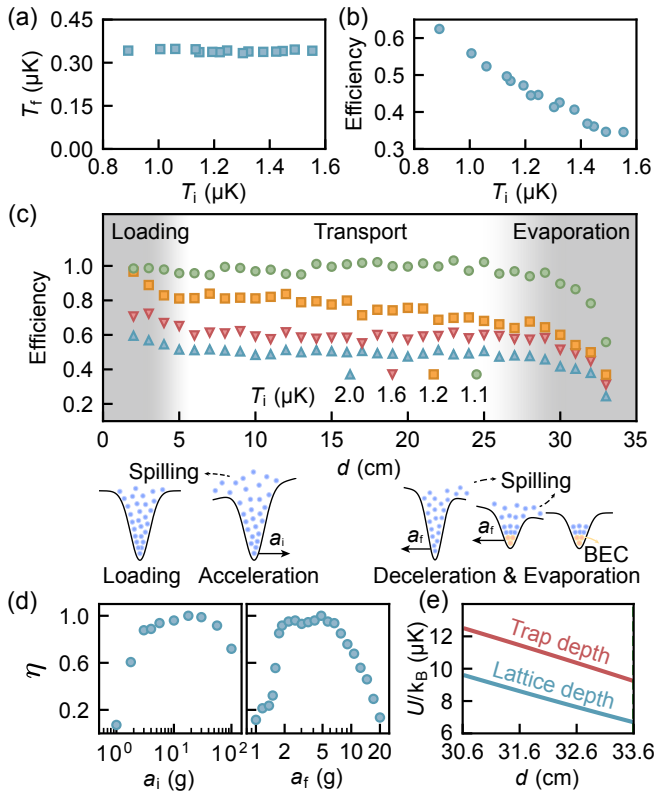


FIG. 2. Transport and cooling mechanism. (a,b) The final temperature and transport efficiency for different initial loading temperatures. The overall transport efficiency increases with decreasing initial temperature. The final temperature depends on the final trap depth rather than the initial loading. (c) The round-trip transport efficiency as a function of transport distance for different initial temperatures. The schematic illustrates the mechanisms of atom loss and cooling during the loading phase as well as the effective evaporative cooling in the final stage. (d) The accelerations and final decelerations in units of the gravitational acceleration g are optimized based on the relative atom number after transport. (e) The trap depth and optical lattice depth at different positions in the final cooling stage.

The second stage spans the transport of approximately 25 cm indicated by the white regime in Fig. 2(c). Both the atom number and temperature remain stable and exhibit a slight decrease during round-trip transport, with the transport efficiency approaching 90%. Atoms with different initial temperatures have almost identical return temperatures, indicating that the temperature during transport is mainly determined by the lattice depth. The dependence of the round-trip temperature on the transport distance is shown in Fig. S5 in the Supplemental Material.

The final evaporative cooling occurs in the last few centimeters of the transport path. The trapping potential is below that of the initial loading stage and decreases substantially with distance (see Supplemental Material for details). The atoms are decelerated by reducing the

frequency difference Δf . The final temperature is mainly determined by the lattice depth at the destination. Total transport efficiency decreases with increasing initial temperature, indicating that hotter atoms are removed during the transport. Fig. 2(e) shows both the trap depth and the lattice depth of the transport lattice decrease, facilitating thermalization and evaporative cooling through the removal of hotter atoms. The right panel of Fig. 2(d) shows the dependence of the relative final atom number on the deceleration. Here, the deceleration is optimized around $a_f \approx 5g$ in the experiment achieving more effective cooling of atoms.

This evaporative cooling and the strong axial confinement of the optical lattice due to the small beam size of the Bessel beams, result in a sufficient phase-space density for subsequent collision thermalization. We managed to transport 3×10^5 atoms at 340 nK to the destination. Due to strong confinement along the transport direction, there are approximately 57 isolated, pancake-shaped two-dimensional clouds detected by the insitu image with random phases as a result of independent collision thermalization during evaporation.

Notably, atoms in each pancake cannot undergo Bose-Einstein condensation due to the quasi-2D geometry ($\hbar\omega_z/(k_B T) \approx 3.5$). Atoms have a similar phase within each pancake but different phases between different pancakes. The temperature of atoms $T = 340$ nK is in between the quasicondensation crossover temperature, $T_c = 1.4$ μK and the Berezinskii-Kosterlitz-Thouless (BKT) transition temperature $T_{\text{BKT}} = 201$ nK [31–33]; see Supplemental Material for details. The quasicondensate fraction in our experiment is $n_{2s}^{(0)}/n = 0.29$, which is further confirmed by the emergence of a narrow peak in 10 ms TOF images.

IV. EMERGENCE OF BEC FROM PHASE SYNCHRONIZATION

Eventually, transferred atoms in each pancake are further loaded from the lattice into a crossed 1064 nm dipole trap in the science chamber with trap frequencies $(\omega_x, \omega_y, \omega_z) = 2\pi \times (121, 73, 142)$ Hz, and potential depth $U_{\text{sci}} \approx 5.5$ μK. Then, atoms are held for variable times, and a BEC emerges from the phase synchronization among the initial quasi-2D pancakes. Similar to the Kibble-Zurek mechanism, phase domains formed in the moving lattice subsequently relax and synchronize through atomic interactions. These interactions help thermalization, synchronize the phases across all pancakes, induce spontaneous breaking of the U(1) symmetry, and eventually lead to the formation of a Bose-Einstein condensate.

Fig. 3 shows bimodal fits to momentum distributions together with representative TOF images after different hold times, revealing the rapid formation of a distinct condensate peak (light blue) from the thermal Gaussian background. This indicates BEC growth through col-

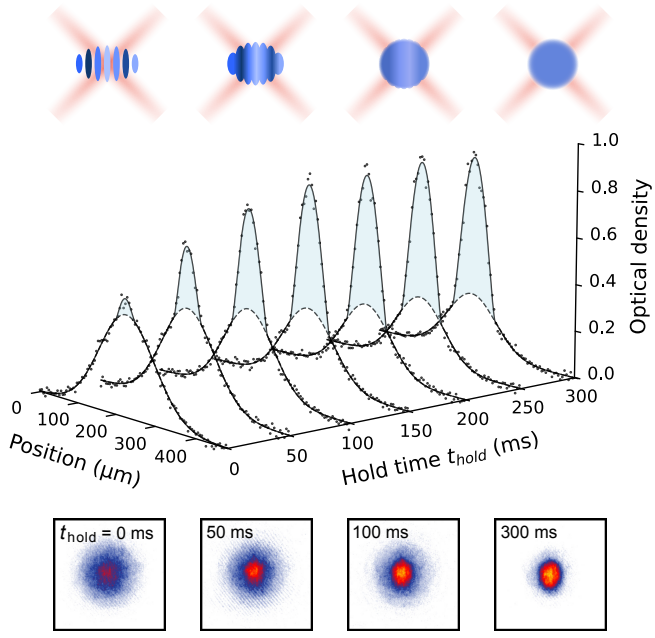


FIG. 3. Emergence of BEC from the phase synchronization. Cold atoms with initially different phases (indicated by different blue colors) are released from the moving lattice to a dipole trap and subsequently synchronized through atomic interactions, resulting in the formation of a Bose-Einstein condensate. Bimodal fits (solid lines) to the momentum distributions at different hold times, with the Gaussian component (dashed lines) representing the thermal atoms, are used to extract the condensate and thermal fractions. The TOF is 20 ms.

lision thermalization in the dipole trap, with the condensate developing rapidly within 150 ms and gradually approaching saturation thereafter.

We calibrate the temperature and condensation throughout the phase synchronization process in Fig. 4. The dependence of temperature T_{thermal} and condensed atom number N_0 on the hold time shows a different mechanism from conventional evaporative cooling. During the first 150 ms, the temperature decreases slowly but the condensed atom number increases rapidly and saturates at approximately 4×10^4 . The final temperature is $T = 172$ nK and the critical temperature for the BEC transition is $T_c = 209$ nK. Fig. 4(b) presents the condensate fraction and the phase-space density (PSD) as a function of hold time, $\text{PSD} = N_{\text{thermal}} (\hbar \bar{\omega} / k_B T)^3$ with $\bar{\omega} = (\omega_x \omega_y \omega_z)^{1/3}$ and the number of thermal atoms N_{thermal} . Interestingly, the PSD increases slowly throughout the process, whereas the BEC fraction grows sharply. Moreover, both the condensate fraction and PSD increase with increasing the total number of transported atoms. The condensate fraction is measured as a function of the total atom number remaining after the 0.3 s hold in Fig. 4(c). With increasing the atom number, both the condensation and PSD increase.

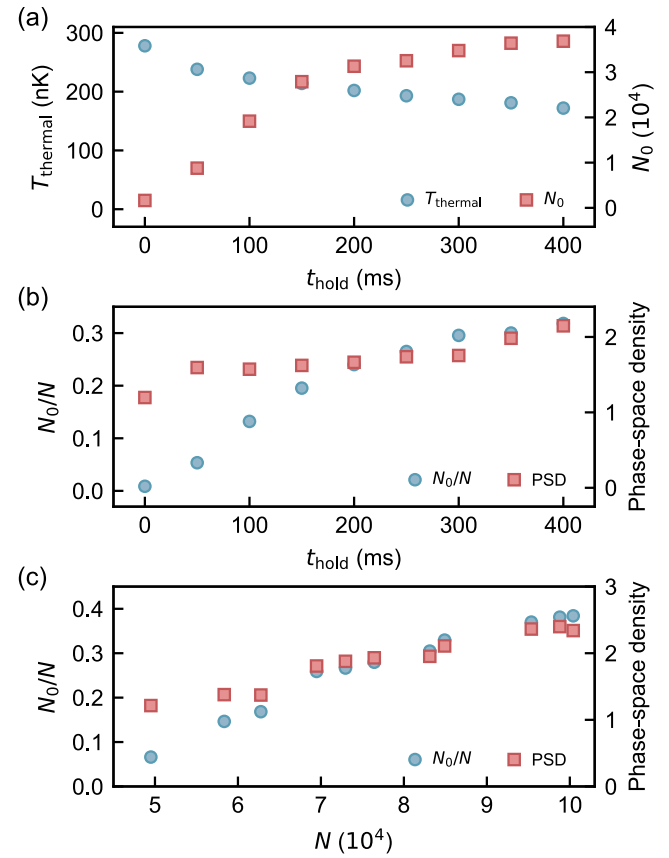


FIG. 4. Benchmark of BEC formation (a) The temperature of the thermal cloud decreases and the condensate fraction increases, with increasing hold time. (b) Corresponding condensate fraction and phase-space density (PSD) extracted from fittings are plotted as a function of hold time. (c) The condensate fraction and PSD as a function of the total atom number remaining after the 0.3 s hold. Increasing the atom number loaded into the moving lattice leads to a higher final condensate fraction and a larger PSD after synchronization.

V. CONCLUSION

We demonstrate rapid optical transport of cold atoms to quantum degeneracy using an optical moving lattice formed by interfering two Bessel beams. A gas of 3×10^5 Yb atoms at 340 nK is transferred over 34 cm in 350 ms with above 60% efficiency and well controlled by tuning the frequency difference between two beams. Effective evaporative cooling of atoms in each pancake is achieved by decelerating the lattice while gradually lowering the trapping potential along the transport path. A gas of 1×10^5 atoms with 40% condensate eventually emerges from the phase synchronization across those pancakes with different phases. This phase synchronization process opens new opportunities to study BKT and BEC transitions. Our rapid and efficient transport demonstrated here paves the way for atom lasers and continuously operated large-scale atomic arrays.

VI. ACKNOWLEDGMENTS

This work was supported by the Quantum Science and Technology-National Science and Technology Major Project (2024ZD0301800), the Beijing Natural Science Foundation (Z240007), the National Natural Science Foundation of China (12374242), and the Scientific Research Innovation Capability Support Project for Young

Faculty (ZY2025014).

VII. DATA AVAILABILITY

The data presented in this work are available on the Peking University Open Research Data Platform.

[1] C. C. Chen, R. González Escudero, J. Minář, B. Pasquiou, S. Bennetts, and F. Schreck, Continuous Bose-Einstein condensation, *Nature* **606**, 683 (2022).

[2] N. C. Chiu, E. C. Trapp, J. Guo, M. H. Abobeih, L. M. Stewart, S. Hollerith, P. L. Stroganov, M. Kalinowski, A. A. Geim, S. J. Evered, *et al.*, Continuous operation of a coherent 3,000-qubit system, *Nature* **646**, 1075 (2025).

[3] R. Tao, M. Ammenwerth, F. Gyger, I. Bloch, and J. Zeiher, High-fidelity detection of large-scale atom arrays in an optical lattice, *Physical Review Letters* **133**, 013401 (2024).

[4] V. M. Schäfer, Z. Niu, J. R. K. Cline, D. J. Young, E. Y. Song, H. Ritsch, and J. K. Thompson, Continuous recoil-driven lasing and cavity frequency pinning with laser-cooled atoms, *Nature Physics* **21**, 902 (2025).

[5] S. S. Yu, J. You, Y. Bao, L. Anderegg, C. Hallas, G. K. Li, D. Lim, E. Chae, W. Ketterle, K.-K. Ni, *et al.*, A conveyor-belt magneto-optical trap of CaF, *Nature Communications* **17**, 1175 (2026).

[6] J. Sauer, K. Fortier, M. Chang, C. Hamley, and M. Chapman, Cavity QED with optically transported atoms, *Physical Review A* **69**, 051804 (2004).

[7] K. Nakagawa, Y. Suzuki, M. Horikoshi, and J. B. Kim, Simple and efficient magnetic transport of cold atoms using moving coils for the production of Bose-Einstein condensation, *Applied Physics B* **81**, 791 (2005).

[8] D. Pertot, D. Greif, S. Albert, B. Gadway, and D. Schneble, Versatile transporter apparatus for experiments with optically trapped Bose-Einstein condensates, *Journal of Physics B: Atomic, Molecular and Optical Physics* **42**, 215305 (2009).

[9] S. Händel, T. P. Wiles, A. L. Marchant, S. A. Hopkins, C. S. Adams, and S. L. Cornish, Magnetic merging of ultracold atomic gases of ^{85}Rb and ^{87}Rb , *Physical Review A* **83**, 053633 (2011).

[10] M. Greiner, I. Bloch, T. W. Hänsch, and T. Esslinger, Magnetic transport of trapped cold atoms over a large distance, *Physical Review A* **63**, 031401 (2001).

[11] W. Hänsel, J. Reichel, P. Hommelhoff, and T. W. Hänsch, Magnetic conveyor belt for transporting and merging trapped atom clouds, *Physical Review Letters* **86**, 608 (2001).

[12] S. Minniberger, F. Diorico, S. Haslinger, C. Hufnagel, C. Novotny, N. Lippok, J. Majer, C. Koller, S. Schneider, and J. Schmiedmayer, Magnetic conveyor belt transport of ultracold atoms to a superconducting atomchip, *Applied Physics B* **116**, 1017 (2014).

[13] T. L. Gustavson, A. P. Chikkatur, A. E. Leanhardt, A. Görlitz, S. Gupta, D. E. Pritchard, and W. Ketterle, Transport of Bose-Einstein condensates with optical tweezers, *Physical Review Letters* **88**, 020401 (2002).

[14] A. Couvert, T. Kawalec, G. Reinaudi, and D. Guéry-Odelin, Optimal transport of ultracold atoms in the non-adiabatic regime, *Europhysics Letters* **83**, 13001 (2008).

[15] M. A. Naides, R. W. Turner, R. A. Lai, J. M. DiSciacca, and B. L. Lev, Trapping ultracold gases near cryogenic materials with rapid reconfigurability, *Applied Physics Letters* **103**, 251112 (2013).

[16] J. Léonard, M. Lee, A. Morales, T. M. Karg, T. Esslinger, and T. Donner, Optical transport and manipulation of an ultracold atomic cloud using focus-tunable lenses, *New Journal of Physics* **16**, 093028 (2014).

[17] D. Schrader, S. Kuhr, W. Alt, M. Müller, V. Gomer, and D. Meschede, An optical conveyor belt for single neutral atoms, *Applied Physics B* **73**, 819 (2001).

[18] S. Schmid, G. Thalhammer, K. Winkler, F. Lang, and J. H. Denschlag, Long distance transport of ultracold atoms using a 1D optical lattice, *New Journal of Physics* **8**, 159 (2006).

[19] T. Klostermann, C. R. Cabrera, H. von Raven, J. F. Wienand, C. Schweizer, I. Bloch, and M. Aidelsburger, Fast long-distance transport of cold cesium atoms, *Physical Review A* **105**, 043319 (2022).

[20] Y. Bao, S. S. Yu, L. Anderegg, S. Burchesky, D. Gonzalez-Acevedo, E. Chae, W. Ketterle, K. Ni, and J. M. Doyle, Fast optical transport of ultracold molecules over long distances, *New Journal of Physics* **24**, 093028 (2022).

[21] J. Trisnadi, M. Zhang, L. Weiss, and C. Chin, Design and construction of a quantum matter synthesizer, *Review of Scientific Instruments* **93**, 083203 (2022).

[22] A. J. Matthies, J. M. Mortlock, L. A. McArd, A. P. Raghuram, A. D. Innes, P. D. Gregory, S. L. Bromley, and S. L. Cornish, Long-distance optical-conveyor-belt transport of ultracold ^{133}Cs and ^{87}Rb atoms, *Physical Review A* **109**, 023321 (2024).

[23] M. J. Pritchard, A. S. Arnold, S. L. Cornish, D. W. Hallwood, C. V. S. Pleasant, and I. G. Hughes, Transport of launched cold atoms with a laser guide and pulsed magnetic fields, *New Journal of Physics* **8**, 309 (2006).

[24] A. L. Marchant, S. Händel, T. P. Wiles, S. A. Hopkins, and S. L. Cornish, Guided transport of ultracold gases of rubidium up to a room-temperature dielectric surface, *New Journal of Physics* **13**, 125003 (2011).

[25] J. Hu, A. Urvoy, Z. Vendeiro, V. Crépel, W. Chen, and V. Vuletić, Creation of a Bose-condensed gas of ^{87}Rb by laser cooling, *Science* **358**, 1078 (2017).

[26] A. Urvoy, Z. Vendeiro, J. Ramette, A. Adiyatullin, and V. Vuletić, Direct laser cooling to Bose-Einstein condensation in a dipole trap, *Physical Review Letters* **122**, 203202 (2019).

- [27] M. Xin, W. S. Leong, Z. Chen, Y. Wang, and S.-Y. Lan, Fast quantum gas formation via electromagnetically induced transparency cooling, *Nature Physics* **21**, 63 (2025).
- [28] X. Li, Y. Wang, L. Yu, and B. Song, Two-color magneto-optical trapping of ytterbium atoms, *Physical Review Applied* **24**, 044039 (2025).
- [29] O. Brzobohatý, T. Čižmár, and P. Zemánek, High quality quasi-Bessel beam generated by round-tip axicon, *Optics Express* **16**, 12688 (2008).
- [30] C. L. Hung, X. Zhang, N. Gemelke, and C. Chin, Accelerating evaporative cooling of atoms into Bose-Einstein condensation in optical traps, *Physical Review A* **78**, 011604 (2008).
- [31] L. Pitaevskii and S. Stringari, *Bose-Einstein Condensation and Superfluidity* (Oxford University Press, 2016).
- [32] D. S. Fisher and P. Hohenberg, Dilute Bose gas in two dimensions, *Physical Review B* **37**, 4936 (1988).
- [33] P. Clade, C. Ryu, A. Ramanathan, K. Helmerson, and W. D. Phillips, Observation of a 2D Bose gas: from thermal to quasicondensate to superfluid, *Physical Review Letters* **102**, 170401 (2009).
- [34] N. Prokof'ev, O. Ruebenacker, and B. Svistunov, Critical point of a weakly interacting two-dimensional Bose gas, *Physical Review Letters* **87**, 270402 (2001)

SUPPLEMENTAL MATERIAL

I. BESSEL BEAMS AND ALIGNMENT

The moving lattice consists of two Bessel beams. The Bessel beams are generated by passing collimated Gaussian beams through axicons. Within a distance $z_{\max} = w_0 / \tan \beta$ after the axicon, the central spot size of the Bessel beam remains almost the same, where w_0 is the incident Gaussian beam waist radius and $\beta = (n - 1)\alpha$ with the axicon apex angle α and the refractive index n . The intensity of the Bessel beam as a function of the radial coordinate ρ and the axial coordinate (along the transport direction) z is given by [29]

$$I(\rho, z) = \frac{4Pk \sin \beta}{w} \frac{z}{z_{\max}} J_0^2(k\rho \sin \beta) \exp\left(-\frac{2z^2}{z_{\max}^2}\right) \quad (\text{S1})$$

where J_0 is the zeroth-order Bessel function of the first kind, P is the power and $k = 2\pi/\lambda$ is the wavevector with the wavelength of the lattice beam λ . The zero-order Bessel spot corresponds to the diffraction-free central lobe, with a radius $\rho_0 \approx 2.405/k \sin \beta = 50 \mu\text{m}$ in our experiment. We detected the profiles of the Bessel beams at different positions after the axicon in Fig. S1(a). We fit the Bessel curve to the measurement and extract the beam size as a function of distance from the axicon z in Fig. S1(b,c). The measurement and theory are in good agreement.

As it is challenging to align two beams passing through two holes with a radius of $50 \mu\text{m}$ over 34 cm distance, we develop a systematic and efficient method for precise long-distance alignment of two counter-propagating

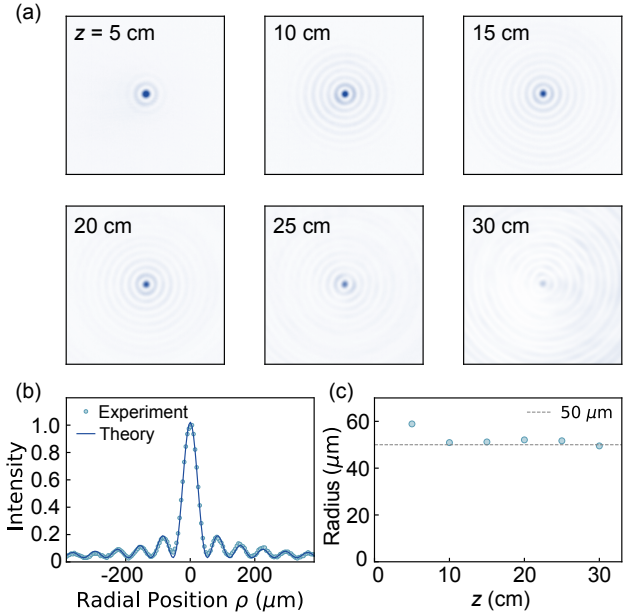


FIG. S1. **Calibration of the Bessel beam.** (a) The measured beam profile of a collimated Gaussian beam with a waist radius of 2.5 mm after transmission through the axicon with an apex angle of $\alpha = 1^\circ$ and a refractive index of $n = 1.5$. (b) The measured intensity (circles) agrees well with the simulation (solid lines). (c) The beam waist of the Bessel beam is almost constant $\sim 50 \mu\text{m}$ along with transport.

Bessel beams, as illustrated in Fig. S2. First, we align the two counter-propagating Gaussian beams to completely overlap in the absence of axicons, and ensure that each beam fully enters the opposite optical isolator. Next, we insert Axicon 1, and simultaneously adjust the preceding pair of mirrors and the axicon itself to produce a uniform Bessel beam capable of independently trapping cold atoms in the crossed dipole trap in the MOT chamber while still entering the isolator. This step relies on different imaging systems in our optical setup, iteratively comparing the positions of the cold atoms in the dipole trap, followed by further optimization of the loading efficiency into the Bessel beam.

Subsequently, we use two cameras behind the mirrors to record the Bessel ring patterns formed by each counter-propagating beam after passing through Axicon 1. Multiple concentric ring images are fitted to determine their central positions. After adding Axicon 2, we ensure that the Bessel beam center on Camera 2 remains unchanged with and without the axicon, guaranteeing that Axicon 2's center aligns with the central spot of Bessel 1 within $\sim 20 \mu\text{m}$. Finally, we adjust the pair of mirrors after Axicon 2 to achieve uniform imaging of the retro-reflected Gaussian 2 beam (passing through both axicons) on Camera 1. Consequently, Bessel 1 is centered through both axicons relative to the atomic position. Empirically, this coarse alignment already enables atomic transport over distances of up to approximately 15 cm.

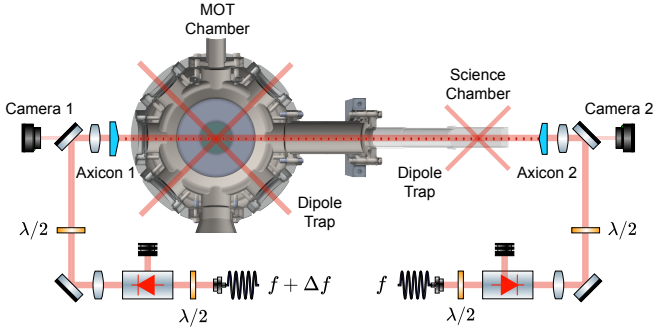


FIG. S2. Experimental details and alignment procedure of two Bessel beams. The Bessel beams are generated from Gaussian beams delivered by fiber couplers and optical isolators, and subsequently expanded to beam waist radii of 2.5 mm and 3 mm in the left and right optical arms, respectively, with the beam profiles monitored by cameras via beam splitters.

Finally, fine alignment is achieved by adjusting the pair of mirrors after Axicon 2 until the cold atoms in the MOT chamber exhibit a pronounced diffraction signal, i.e., the Kapitza-Dirac (KD) effect, induced by the moving lattice. This procedure ensures precise alignment in the MOT chamber. At this stage, atoms can be reliably transported to the science chamber. Further optimization of the transport efficiency, together with fine adjustments of Axicon 2 and the subsequent pair of mirrors, ultimately achieves precise alignment of the two Bessel beams.

II. TRANSPORT EQUATIONS

Here we provide the detailed calculation of the moving optical lattice. The complex amplitudes of the two beams are given by

$$\begin{aligned} E_1(z, \rho, t) &= E_1(z, \rho) e^{i(\omega + \Delta\omega)(t - z/c)}, \\ E_2(z, \rho, t) &= E_2(z, \rho) e^{i\omega(t + z/c)}, \\ E_{\text{total}}(z, \rho, t) &= E_1(z, \rho, t) + E_2(z, \rho, t), \end{aligned} \quad (\text{S2})$$

where ω is the optical angular frequency of beam 2, and $\Delta\omega$ is the angular frequency difference between two beams. The intensity distributions of the two Bessel beams read

$$\begin{aligned}
I_1(z, \rho) &= E_1(z, \rho, t) E_1^*(z, \rho, t) \\
&= \frac{4P_1 k \sin \beta}{w_1} \frac{z}{z_{\max 1}} J_0^2(k \rho \sin \beta) \exp \left(-\frac{2z^2}{z_{\max 1}^2} \right), \\
I_2(z, \rho) &= E_2(z, \rho, t) E_2^*(z, \rho, t) \\
&= \frac{4P_2 k \sin \beta}{w_2} \frac{l-z}{z_{\max 2}} J_0^2(k \rho \sin \beta) \exp \left(-\frac{2(l-z)^2}{z_{\max 2}^2} \right), \tag{S3}
\end{aligned}$$

where P_i and w_i are the power and waist of the incoming Gaussian beams after each axicon, $z_{\max i} = w_i / \tan(\beta)$ is the diffraction-free propagation range, and l is the distance between the two axicons.

The interference of the two Bessel beams produces the intensity distribution given by $I(z, \rho, t) = E_{\text{total}}(z, \rho, t)E_{\text{total}}^*(z, \rho, t)$. The resultant intensity is the sum of the individual beam intensities and an interference term,

$$I(z, \rho, t) = I_1(z, \rho) + I_2(z, \rho) + 2\sqrt{I_1(z, \rho)I_2(z, \rho)} \cos(\Delta\phi), \quad (\text{S4})$$

where the phase difference is $\Delta\phi = \Delta\omega t - 2kz$. Therefore, the lattice transport velocity is as follows,

$$v = \frac{1}{2} \lambda \cdot \Delta f \quad (S5)$$

The dipole potential of the moving lattice is proportional to the light intensity,

$$U_{\text{pot}}(z, \rho, t) = -\frac{3\pi c^2}{2\omega_0^3} \left(\frac{\Gamma}{\Delta}\right) I(z, \rho, t) = -\alpha I(z, \rho, t) \quad (\text{S6})$$

where α is the atomic polarizability. In the axial direction along the transport direction, the lattice potential is sinusoidal and its depth is

$$U_{\text{axial}}(z) = -4\alpha\sqrt{I_1(z)I_2(z)}. \quad (\text{S7})$$

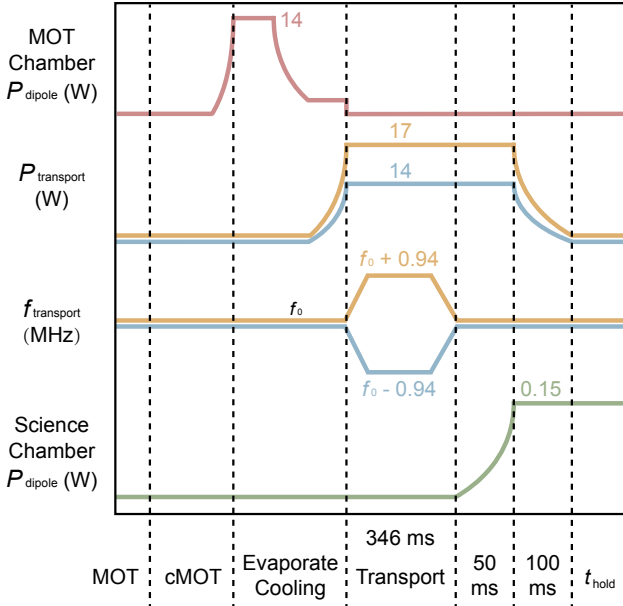
For the radial direction, perpendicular to the transport direction, the optical potential traps the atoms to compensate the gravity. The potential depth is determined by the total light intensity,

$$U_{\text{radial}}(z) = -\alpha \left[I_1(z) + I_2(z) + 2\sqrt{I_1(z)I_2(z)} \right]. \quad (\text{S8})$$

Fig. S4(a) shows calculated axial lattice and the radial trapping potential over the whole transport.

III. EXPERIMENTAL SEQUENCE AND PRECISE TRANSPORT CONTROL

Fig. S3 shows the experimental sequence. A gas of 1×10^8 ^{174}Yb atoms at $18 \mu\text{K}$ is prepared by Zeeman slowing and two-color magneto-optical trapping [28]. The

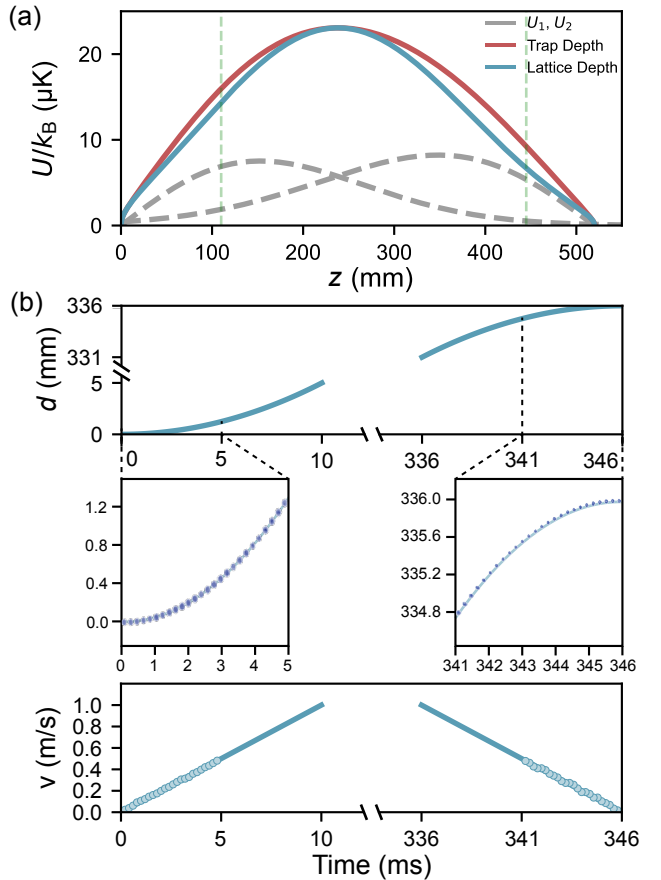


atoms are further compressed via a compressed MOT stage (cMOT) and transferred into a crossed 1064 nm optical dipole trap, with each beam having a power of 14 W. The dipole trap is exponentially ramped up in 10 ms and the temperature of atoms is controlled by the endpoint of evaporative cooling in the dipole trap. Subsequently, the moving lattice is ramped adiabatically to transfer atoms from the dipole trap into the moving optical lattice.

Next, the frequencies of the two counter-propagating transport beams are tuned in time to move the optical lattice and transport the atoms to the science chamber within 350 ms. The transport frequencies are tuned by double-pass AOMs and the two beams are symmetrically detuned by ± 0.94 MHz (Fig. S3). The total frequency difference between two beams $\Delta f = 1.88$ MHz. This sets the lattice velocity $v = \lambda\Delta f/2 = 1.0$ m/s.

The two dipole beams are ramped up to 150 mW within 50 ms, followed by ramping down the two transport beams in 100 ms. Finally for the stage of phase synchronization, atoms are held in the dipole trap for different hold times t_{hold} .

Crucially, the transport of cold atoms is well controlled by the frequency difference between two Bessel beams, including 10 ms linear acceleration to 1 m/s, 326 ms constant-velocity transport, and 10 ms deceleration to rest in Fig. S4b. The atomic position during acceleration and deceleration phases is detected in the MOT and science chambers respectively. The measured center of mass in the acceleration and deceleration stages agrees well with the designed trajectories with correlation coefficients $r^2 > 0.9999$ for both stages. We estimate that



the actual accuracy of transport is about 2 μ m over the whole transport.

IV. ROUND-TRIP TRANSPORT

Fig. S5 shows the temperature of atomic clouds for different initial temperatures after round-trip transport to different positions. Similar to Fig. 2(c) in the main text, the transport and evaporation stages are separated. During the second phase of transport, the temperature gradually decreases, while in the final phase, it drops significantly, indicating a collision thermalization in the evaporative cooling. Moreover, for atoms with different initial temperatures, the round-trip temperatures are almost the same, indicating that the temperature is governed by the local trap depth.

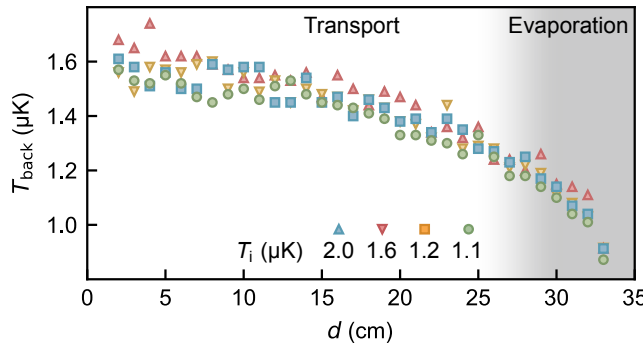


FIG. S5. **Temperature after round-trip transport.** The final temperature is independent of the initial loading temperature and is determined by the trap potential.

V. THERMOMETRY AND CONDENSATION

The strong lattice confinement along the moving lattice results in a series of quasi-2D pancakes, following the 2D criterion $\hbar\omega_z/(k_B T) \approx 3.5$, where ω_z is the axial trap angular frequency, \hbar is the reduced Planck constant, k_B is the Boltzmann constant, and the temperature after transport is $T = 340$ nK. In this regime, the coupling between pancakes is frozen and the isolated 2D pancakes cannot have true long-range order. To quantify phase coherence and quasicondensation within each pancake, we consider two characteristic temperatures: The quasicondensation crossover temperature \tilde{T}_c , and the Berezinskii-Kosterlitz-Thouless (BKT) transition temperature T_{BKT} [31–33].

Based on the Landau quasiparticle theory for vanishing 2D superfluid density n_{2s} , the critical temperature from a thermal gas to a quasicondensate gas is

$$\tilde{T}_c = \frac{2\pi\hbar^2 n_2}{k_B m} \left[\ln\left(\frac{\hbar^2 n_2}{m^2 c^2}\right) \right]^{-1}, \quad (\text{S9})$$

where c is the sound speed of interacting atoms in two dimensions, m is the atomic mass and n_2 is the peak 2D number density in each pancake. We calculate c from the equation of state using $mc^2 \approx \mu \approx g_{2D} n_2$, where μ is the chemical potential and g_{2D} is the effective 2D coupling constant.

The BKT transition temperature is

$$T_{\text{BKT}} = \frac{2\pi\hbar^2 n_2}{k_B m} \left[\ln\left(\frac{C\hbar^2}{mg_{2D}}\right) \right]^{-1}, \quad (\text{S10})$$

with $C \approx 380$ [34]. In our experiment, the final gas contains $N = 3 \times 10^5$ atoms distributed across 57 pancakes, yielding an average atom number per pancake $N_p = 5.3 \times 10^3$. We estimate $\tilde{T}_c = 1.4$ μK and $T/\tilde{T}_c = 0.24$, while $T_{\text{BKT}} = 201$ nK and $T/T_{\text{BKT}} = 1.7$. Thus the temperature of atoms in each pancake is close to the BKT transition but below the quasicondensation crossover temperature.

Correspondingly, we estimate the quasicondensate fraction in each pancake, i.e. the “bare” superfluid fraction, $n_{2s}^{(0)}/n_2 = 0.29$ at $T = 340$ nK, where the superscript (0) denotes the Landau estimate without considering vortices. We further confirm it by observing a condensed momentum peak after a short TOF along the direction perpendicular to the lattice in Fig. S6.

After transferring atoms into the shallow crossed dipole trap, atomic interactions help synchronize phases across pancakes. During this collision thermalization, rapid phase synchronization leads to the emergence of a global BEC on a timescale of 100 ms. The critical temperature for the BEC transition in the harmonic trap is

$$T_c = \frac{\hbar\bar{\omega}}{k_B} \left(\frac{N}{\zeta(3)} \right)^{1/3}, \quad (\text{S11})$$

where $\bar{\omega} = (\omega_x \omega_y \omega_z)^{1/3}$ is the average trap frequency and ζ is Riemann zeta function. The critical temperature for BEC transition in the final dipole trap is $T_c = 209$ nK. We achieve a gas of $N = 10^5$ atoms at a temperature of $T = 172$ nK after phase synchronization. The measured condensate fraction is approximately 40%, in agreement with the estimate $N_0/N = 1 - (T/T_c)^3 = 46\%$ based on temperature.

Fig. S6 shows the thermometry of atoms in the pancake and in the dipole trap after phase synchronization. For the pancake, there is a clear difference between the cut of 10 ms TOF along the transport direction (horizontal) and the direction perpendicular to transport (vertical). In contrast to the vertical direction, the quasicondensate fraction of the horizontal direction is almost zero. We fit the bimodal curve (solid lines) to the data to extract the quasicondensate fraction 0.28, consistent with the simulated value $n_{2s}^{(0)}/n_2 = 0.29$. For the atoms in the dipole trap after a hold of 0.3 s, condensation emerges in both horizontal and vertical directions with a condensate fraction of 48% and 43% respectively in the 20 ms TOF image in Fig. S6(c,d).

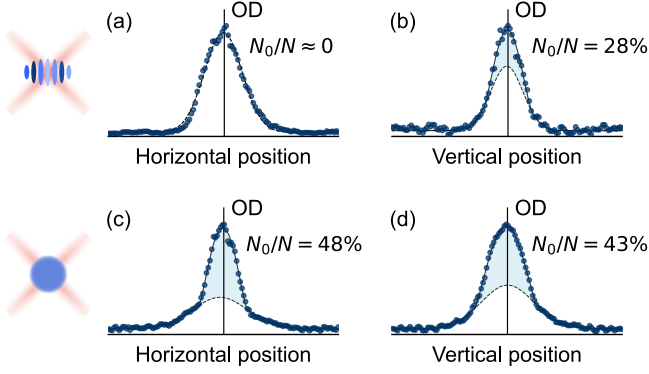


FIG. S6. Momentum distributions of atoms in the pancake after transport and in the dipole trap after phase synchronization. (a,b) Cuts along the transport direction (horizontal) and perpendicular to the transport direction (vertical) of the momentum distribution of atoms in pancakes after transport. In contrast to the vertical momentum distribution which shows a clear bimodal feature (solid lines) and quasicondensation (light blue), the horizontal momentum distribution remains thermal and is well fitted by a Gaussian profile (dashed lines). The extracted quasicondensate fraction from the bimodal fitting (solid lines) is 0.28, in good agreement with the estimate $n_{2s}^{(0)}/n_2 = 0.29$. (c,d) After phase synchronization, both the horizontal and vertical distributions exhibit clear bimodal features with condensate fractions of $N_0/N = 48\%$ and 43% , in good agreement with the estimate $N_0/N = 46\%$. TOF are 10ms and 20ms for (a,b) and (c,d) respectively.